# ACTIVE CONTROL OF A VARIABLE SPEED ROTOR DRIVETRAIN SYSTEM USING ELECTRIC VARIATORS

J. Koch*, A. Poks†, Prof. I. Yavrucuk*

* Institute of Helicopter Technology and VTOL, Technical University of Munich, D-85748 Garching, Germany
† Institute of Mechanics and Mechatronics, Vienna University of Technology, AT-1060 Vienna, Austria

Abstract

The integration of a variable speed rotor system in rotorcraft has the potential to improve power efficiency under certain flight conditions. In this work, a continuously variable transmission is implemented by incorporating electrical variators. The dynamics of the drivetrain shaft under variable speed is analyzed by using a multi-software co-simulation environment. An innovative adaptive control strategy is developed to address shaft vibration issues utilizing the highly dynamic variators.

Keywords

Rotorcraft Efficiency Gain; Drivetrain Shaft Dynamics; Continuously Variable Transmission

## NOMENCLATURE

### Symbols

| | | |
|---|---|---|
| $1/rev$ | per rotor revolution | - |
| $A$ | rotor disk area | $m^2$ |
| $\alpha$ | angle of attack | deg |
| $b$ | chord | m |
| $c_l$ | section lift coefficient | - |
| $C_T$ | thrust coefficient | - |
| $C_T/\sigma$ | blade loading | - |
| $D^{us}$ | unsteady drag force | N/m |
| $L^{us}$ | unsteady lifting force | N/m |
| $M^{us}_{NP}$ | unsteady pitching moment | N |
| $Ma$ | Mach number | - |
| $\mu$ | advance ratio | - |
| $\Omega$ | rotor rotational speed | rad/s |
| $\omega_1$ | pitch rate of airfoil | rad/s |
| $P_{shaft}$ | shaft power | W |
| $R$ | blade radius | m |
| $\rho$ | density | $kg/m^3$ |
| $\sigma$ | rotor solidity | - |
| $T$ | shaft torque | Nm |
| $\theta$ | pitch angle of blade | deg |
| $t_{trans}$ | transition time | s |
| $V_{tip}$ | blade tip speed | m/s |

### Indices

| | |
|---|---|
| opt | optimal |
| ref | ref |

### Abbreviations

| | |
|---|---|
| CS | Compound Split |
| FFT | Fast Fourier Transform |
| MCP | Maximum Continuous Power |
| NDARC | NASA Design and Analysis of Rotorcraft Software |
| TSE | Turboshaft Engine |



doi: 10.25967/610302

## 1. INTRODUCTION

Recently, research on variable main rotor speed for different helicopter configurations is performed. The concept is driven by the possibility to reduce noise and vibration, extend range and reduce environmental impact by improved power efficiency, thus enhancing overall helicopter performance. This paper focuses on potential power savings by adjusting the main rotor speed depending on the actual flight state.
It is shown that the optimal drive train concept providing speed variation is influenced by the specific helicopter configuration and its use case. A dual-speed, clutched stage gearbox is particularly suitable for tilt-rotor concepts, whereas continuously variable transmission is especially beneficial for utility helicopter applications [1]. The study shows that a maximum additional empty weight of up to 450 kg for maritime SAR mission and up to 200 kg for troop transport mission can be achieved from fuel savings due to variable main rotor speed. Here the UH-60A with a classical single main-rotor/tail-rotor design is chosen as reference for the continuous variable gear design proposed in this paper. A UH60-A study performed with the conceptual design tool NDARC shows that power savings up to 20 % are possible by varying the main rotor speed in the range from −30 % to +10 % [2], see fig. 4.
The continuous variable transmission is realized by two compound split modules (CS), with one integrated into the power path of each turboshaft engine. Each CS consists of two nested planetary gear stages and two electrical variators. By adjusting the rotational speed of the variators, the overall gear ratio of the entire drive train can be changed. For further details on the concept, please refer to reference [3].

The scope of the present paper involves a coupled simulation approach of the main rotor and drive train together. Recent research on rotor-drive train interaction reveals that relevant coupling effects of the drive shaft have to be considered. An analytical, simplified model of the coupled rotor, engine and drive train is derived in Ref. [4] under neglect of the rotor aerodynamics. It is found that the fundamental collective lag mode of a four bladed articulated rotor has the strongest coupling with the engine/drive train. In contrast, the differential collective, regressing and progressing lag modes do not couple with the drive train since they exert no summed torque about the rotor hub.
In Ref. [5], a modally reduced torsional drive train system is coupled to the UH-60A main rotor. It reveals a decrease in the chordwise blade bending moments and a reduction of the 8/rev shaft torque due to the coupling.
Weiss et al. investigates the influence of the drive train especially for a hingeless rotor [6]. Analogous to Ref. [4], it is found out that the drive train significantly influences the collective lag modes. The physical effect of the coupling is linked to the drive train inertia as well as the drive train stiffness. In his dissertation, Weiss validates this also for the articulated UH-60A rotor [7].

## 2. METHODOLOGY

To investigate the drive train dynamics, a co-simulation environment consisting of turboshaft engine (TSE), compound split module (CS) and main rotor is established. A detailed mathematical model of the GE T700-701C turboshaft engine that is used in the UH-60 helicopter was derived earlier within the framework of this project. It essentially describes the dynamics of the compressor spool and the power spool using the principle of angular momentum. For more details on the model, please refer to [8]. Since the scope of this paper is the dynamics of the compound split gear and the main rotor, the dynamics of the turboshaft engine are neglected. The engine is considered to be a stationary power source operating at a fixed speed.

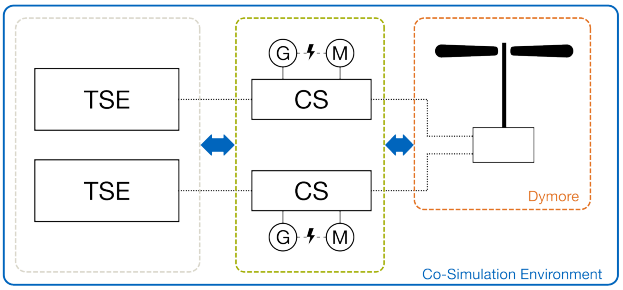


FIG 1. Scheme of the drive train co-simulation environment consisting of turboshaft engine (TSE), compound split module (CS) and main rotor

The model of the compound split gear describes the dynamics of the gear shafts, i.e. sun wheel, planetary carrier, ring gear and the electrical machines of the variators. To derive a state space formulation of the CS, the method of Lagrangian mechanics is used. The derivation of the mathematical model is explained in section 4.
A detailed model of the main rotor is required to study the coupled dynamics of the drive train. The comprehensive analysis tool Dymore is used for this purpose. The implementation of the UH60 similar main rotor is described in section 3.
Because the requirements for modeling the rotor and drive train system are particularly specific and multidisciplinary, a dedicated framework has to be developed. For this purpose, MATLAB Simulink is chosen as the common simulation environment. All three components of the simulation are modeled in this software. The first-order differential equations of the CS are implemented directly in a Simulink subsystem, as well as the modeling of the turboshaft engine. The Dymore source code is originally written in C. The MATLAB Executable (MEX) feature is used for integration into Simulink. This API provides a seamless interface for using C code within Simulink.

The main Dymore functions can therefore be used directly as if they were built-in functions, referred to as "Symore".

## 3. ROTOR MODEL

The modeling of the main rotor is performed using the simulation tool Dymore. It is a finite element based multibody dynamics code with integrated rotor aerodynamics modeling to capture rotor blade elasticity.
The structure of the rotor blades is modeled with the geometrically exact beam theory developed by Bauchau [9]. Cross-sectional structural properties of the blade serve as input for the one-dimensional beam analysis.
The inflow of the rotor is captured using the implementation of the Peters et al. dynamic inflow model included in Dymore [10]. The effects of the unsteady wake in the rotor plane are represented by means of a state-space formulation. The inflow velocity is determined by discretizing the rotor disk in radial and angular direction using Fourier series expansion for the azimuth. For the simulation of the UH60-similar main rotor, the inflow is discretized using 12 modes, corresponding to 91 states. This was chosen to fit to the radial discretization of the blade airloads by 81 airstations and a timestep of $\Delta t = 0.001\,\mathsf{s}$, leading to an azimuthal resolution of 232 steps per revolution at nominal rotor speed of $\Omega_{ref} = 4.3\,\mathsf{Hz}$.
Since the focus is on the analysis of transient speed variation processes, a suitable aerodynamics model is integrated in order to be able to capture relevant transient effects that affect loads arising during switching processes. The steady airloads are computed with the table-look-up method providing airfoil lift, drag and moment coefficients. The UH60 blade consists of the SC1095 airfoil in the inner and outer section and the cambered SC1094R8 airfoil between $0.47R$ and $0.85R$ for increased maneuverability [11]. The calculation of the airloads is performed at the 81 discrete, radially distributed airstations, taking into account the corresponding airfoil. The airstations are rigidly connected to the beam model of the rotor blade and thus serve as the interface between the structural and aerodynamic models. The airloads are transmitted to the beam, while the nodal points experience the displacements and velocities resulting from the FEM analysis, which are considered for the unsteady aerodynamics. In addition to the steady airloads, an unsteady part is superimposed, obtained by the Peters model [12]. The model is generally defined for flexible profiles. However, for the implementation in the simulation environment, a rigid 2D cross-section is assumed, which can be considered as a good approximation. This leads to simplified formulas for the airloads around the aerodynamic center governed by the pitch rate $\omega_1$, pitch acceleration $\dot{\omega}_1$ and acceleration of the incident flow perpendicular to the chord $\dot{v}_{a3}$:

$$L^{us}_{\tilde{a}_3} = a_0 \rho b^2 U_2 \omega_1 - a_0 \rho \frac{b^2}{2} \dot{v}_{a3} \tag{1a}$$

$$D^{us}_{\tilde{a}_2} = 0 \tag{1b}$$

$$M^{us}_{NP} = -a_0 \rho \frac{b^4}{16} \dot{\omega}_1 - \frac{b}{2} L^{us} \tag{1c}$$

where $\rho$ is the density, $b$ is the chord, $U_2$ denotes the component of the incident flow parallel to the chord and $a_0$ corresponds to the theoretical value of the lift curve slope, $2\pi$.

### 3.1. Power Savings

From a physical point of view, the most efficient rotor is optimized for both induced and profile power, referred to as optimum rotor. This is achieved when each blade section operates at optimum lift-to-drag ratio $L/D$, corresponding to an optimum angle of attack $\alpha_{opt}$. In practical blade designs, not all blade sections can operate at $\alpha_{opt}$, but there is an optimal pitch angle $\theta_{opt}$ for which the average lift-to-drag ratio of the entire blade is optimized.
The lift-to-drag ratio over angle of attack for the two

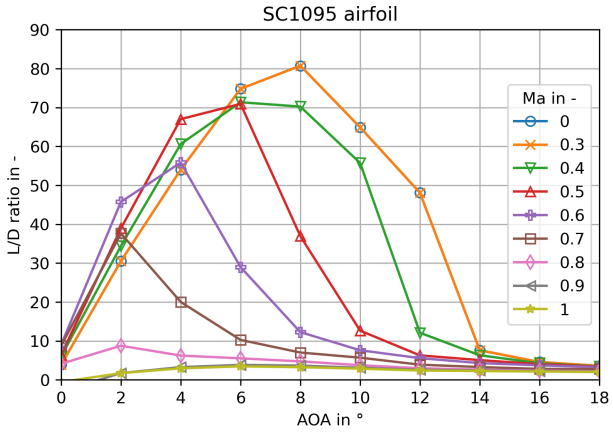


FIG 2. L/D ratio of SC1095 airfoil

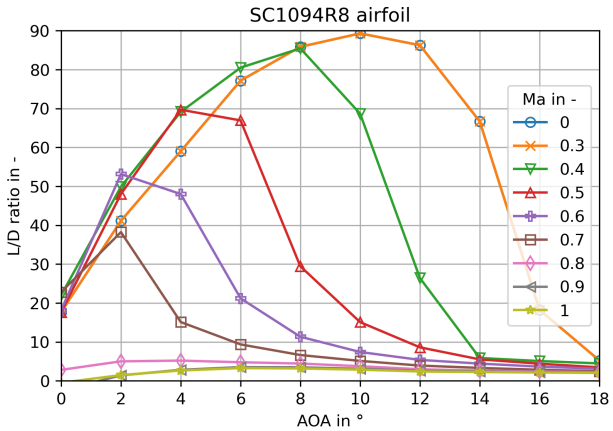


FIG 3. L/D ratio of SC1094R8 airfoil

airfoils of the UH60 blade is shown in fig. 2 and fig. 3. It can be seen that the optimum angle of attack

$\alpha_{opt}$ is dependent on the flow velocity, for higher mach number, $\alpha_{opt}$ decreases to smaller values:

$$(2) \quad \left(\frac{L}{D}\right)_{opt} = \left(\frac{c_l}{c_d}\right)_{opt} = f(Ma) \mid \alpha_{opt} = f(Ma)$$

By means of the blade element theory, a proportional relation between the blade loading $C_T/\sigma$, describing the ratio of the rotor thrust coefficient to the solidity, and the mean lift coefficient $\bar{c}_l$ of the entire blade can be established:

$$(3) \quad \frac{C_T}{\sigma} = \frac{T}{\rho\sigma A\left(\Omega R\right)^2} \quad \propto \bar{c}_l$$

In conclusion, a rotor operating at optimum mean lift coefficient $\bar{c}_{l_{opt}}$ with best lift-to-drag ratio corresponds to one optimum blade loading $(C_T/\sigma)_{opt}$. For the UH60, the design blade loading lies in the range between 0.09 to 0.1. As a consequence, tip speed or rotor speed has to be increased for high blade loading flight conditions and decreased for low blade loading flight conditions in order to get back to the design blade loading with best efficiency.

In the scope of the preceding project VARISPEED I, a power efficiency study regarding variable rotor speed over the whole flight envelope of the UH60 was performed using the conceptual design tool NDARC, c.f. fig. 4. Possible power savings at optimal rotor speed were investigated at discrete flight states in the flight envelope, spanned by the advance ratio $\mu_{ref}$ and the blade loading $(C_T/\sigma)_{ref}$. The $_{ref}$ subscript denotes the normalization with reference tip speed $\Delta V_{tip_{ref}} = 221\,\mathrm{m\,s^{-1}}$ instead of the actual varied tip speed for better comparison of the different flight states. The previously derived trend of decreased rotor speed at low blade loading and increased rotor speed at high blade loading for optimum efficiency is clearly apparent in fig. 4b. Equation 3 shows that the blade loading is proportional to thrust and inversely proportional to density, $C_T/\sigma \propto T \propto 1/\rho$. This means that the same optimum rotor speed has to be achieved when thrust is increased as when density is decreased by the same relative amount. From fig. 4a, it is also apparent that the optimum blade loading is decreasing with increasing advance ratio or mach number, since the blade loading with no possible power saving decreases from 0.1 in hover to 0.09 in high speed flight condition. Considering eq. 2, the following causal chain can be derived:

$$(4) \quad Ma\uparrow \rightarrow \alpha_{L/D_{opt}}\downarrow \rightarrow \bar{c}_{l_{opt}}\downarrow \rightarrow \left(\frac{C_T}{\sigma}\right)_{opt}\downarrow$$

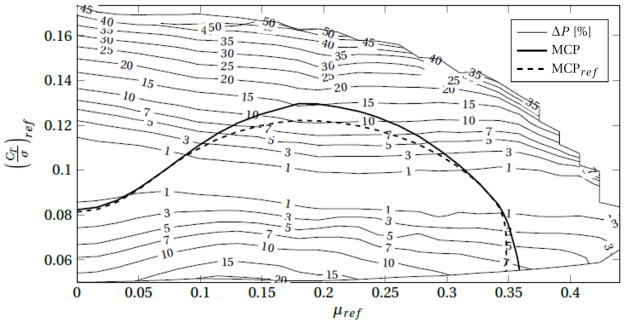


(a) power savings $\Delta P$

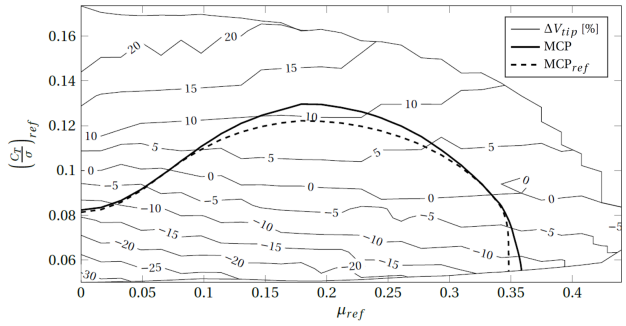


(b) optimum tip speed $\Delta V_{tip}$ respectively rotor speed $\Delta\Omega$

FIG 4. possible power savings (a) and corresponding optimum rotor speed (b) within UH60 flight envelope, taken from [2]

In contrast to the low-fidelity NDARC study, which was performed only for discrete flight states using surrogate models, the focus of the present work is on time-transient rpm change operations using the high-fidelity simulation tool Dymore. To verify the possible power savings obtained from NDARC, specific points in the flight envelope are simulated with Dymore. In general, the Dymore simulation results show the same trends obtained with NDARC. The absolute power savings computed with Dymore are underestimated by 1 % to 5 % compared to NDARC. Next to the differences in the modeling, this could arise from the calculation of the power requirement. While NDARC considers transmission and accessory losses for the total power consumption, Dymore only takes into account the main rotor shaft power calculated from shaft torque and rotor speed, $P_{shaft} = T \cdot \Omega$. For the analysis of time-transient rotor speed switching, the next section considers a case with low blade loading and reduced rotor speed, and a case with high blade loading and increased rotor speed, for both of which the largest possible power savings are identified.

### 3.2. Transient Rotor Speed Variation

For the investigation of transient changes in rotor speed, the fanplot is considered to be an important analytical measure. It reveals regions in the variable speed range, where resonance of blade eigenmodes could occur due to the operation near higher harmonics of the rotor speed. The fanplot of the UH60 similar rotor modeled in Dymore is shown in fig. 5. The plot is generated by a static structural analysis of a single blade without considering aerodynamic effects. Centrifugal forces are applied to the blade in a quasi-stationary manner for each distinct rotor speed level. The continuously variable transmission allows the rotor speed to be varied between 75 % to 110 % percent of the reference rotor speed. For increasing rotor speed, the fanplot does not show any

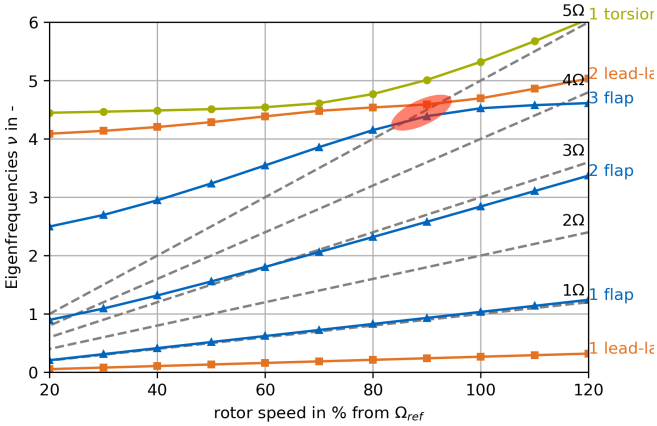


FIG 5. fanplot of the Dymore rotor

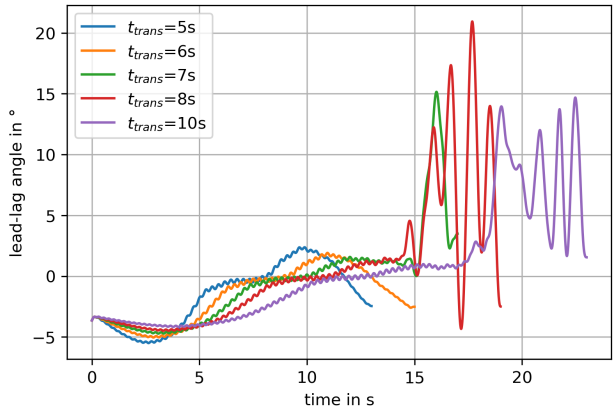


FIG 7. filtered lag angle at different transition times

critical resonance crossings of the eigenmodes. When slowing down the rotor, an interference between the third flapping mode and the second lag mode with the fifth rotor harmonic is observed at 86 % $\Omega_{ref}$ resp. 92 % $\Omega_{ref}$, marked red in fig. 5.
To investigate the resonance effects in the identified range, a transient rotor speed variation simulation is performed using Dymore. A forward flight condition with advance ratio of $\mu = 0.15$ is used to account for aerodynamic effects due to the far field flow. The rotor speed is varied from 100 % $\Omega_{ref}$ to 80 % $\Omega_{ref}$ using a half-period cosine function to smooth the start and end of the switching process. Since it is expected

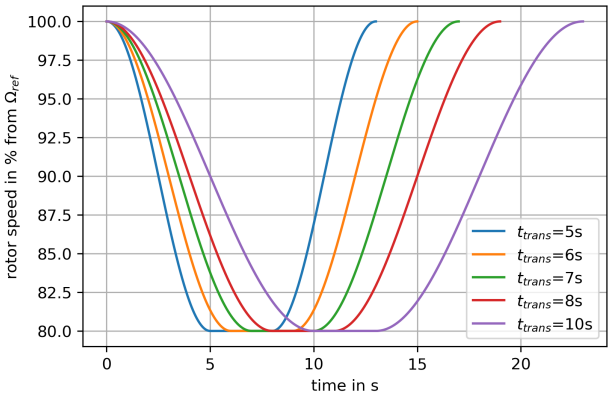


FIG 6. rotor speed curves for different transition times

that faster passage through the resonance point can suppress the rising structural oscillations, simulations using various transition times are performed. The resulting rotor speed curves are shown in fig. 6.
The corresponding blade lag angle is shown in fig. 7. It is measured at the lag hinge on the blade attachment. A Butterworth filter with a cut-off frequency of 2 Hz is applied to the sensor signal to suppress the 1/rev oscillation for better readability. It is noticeable that for transition times up to 6 s, the lag angle remains within an acceptable range. By further increasing the transition time, i.e. slowing down the passage of the resonance crossing, the lag oscillation is excited to an unacceptable level where the lag damper fails. The rotor speed at which resonance starts is identified to be 87 %-89 % (c.f. fig. 6), which corresponds to the resonance crossing of the third flap and second lag mode observed in the fanplot in fig. 5. Remarkably, resonance only occurs when accelerating the rotor from 80 % $\Omega_{ref}$ to 100 % $\Omega_{ref}$, not when slowing it down from 100 % $\Omega_{ref}$ to 80 % $\Omega_{ref}$. This non-linear resonance behavior was also observed by Chandrasekaran in [13].
It has to be noted that these simulations were performed using the steady aerodynamic model described at the beginning of sec. 3. Further simulations taking into account additional unsteady aerodynamic effects with the Peters model (cf. eq. 1) showed that no resonance occurred in this case. The structural motion of the blade is therefore strongly influenced by the underlying aerodynamic model. The unsteady effects apparently lead to an additional damping of the lag motion.

In order to examine the behavior of the shaft torque during rotor speed variation, two specific cases with low and high blade loading condition are considered. The flight state with the most possible power savings at reduced rotor speed was identified for blade loading $C_T/\sigma = 0.05$ and advance ratio $\mu = 0.1$, corresponding to an optimum rotor speed of $\Omega_{opt} = 80\,\%\ \Omega_{ref}$. For this flight condition, the rotor speed was varied following the same method illustrated in fig. 6. The included trim algorithm keeps the thrust constant during rotor speed variation by adjusting the pitch angle of the blades, yielding to a variation of the shaft torque. The response of the shaft torque as the rotor speed varies is shown in fig. 8. The signal was filtered using a Butterworth filter to eliminate 4/rev oscillations to improve readability. The lower section of the chart indicates the rotor's slowdown to $\Omega_{opt} = 80\,\%\ \Omega_{ref}$ (left arrow) , whereas the upper part displays acceleration to the reference rotor speed (right arrow). Again, simulations with different rotor speed time transients were conducted. For a transition time shorter than $t_{trans} = 3s$, the shaft torque becomes negative, indicating that a braking torque would have to be applied to achieve such brief slowdown of the rotor. To

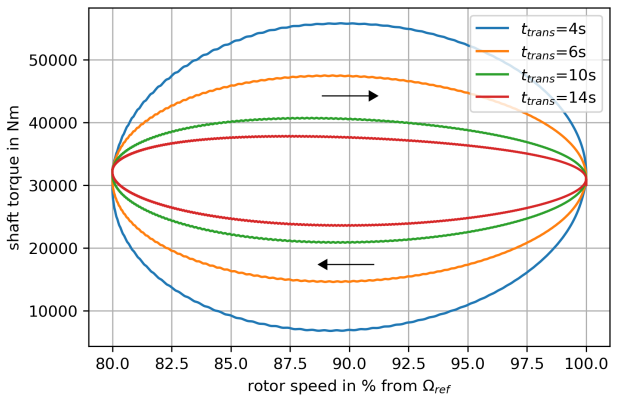


FIG 8. shaft torque during rotor speed variation for low blade loading condition, $C_T/\sigma = 0.05$ and $\mu = 0.1$

quantify the power savings, the shaft power is calculated by multiplying shaft torque with the rotor speed, $P_{shaft} = T \cdot \Omega$. As fig. 8 indicates, the shaft torque at 80 % $\Omega_{ref}$ is only marginally higher than that at reference rotor speed, resulting in a power reduction of $\Delta P_{shaft} = 16.25\,\%$.
Next to a flight state with optimum rotor speed below reference speed, a high blade loading condition with increased rotor speed is considered. For $C_T/\sigma = 0.125$ and an advance ratio of $\mu = 0.2$, the optimum rotor speed was identified to be $\Omega_{opt} = 110\,\%\ \Omega_{ref}$. Fig. 9

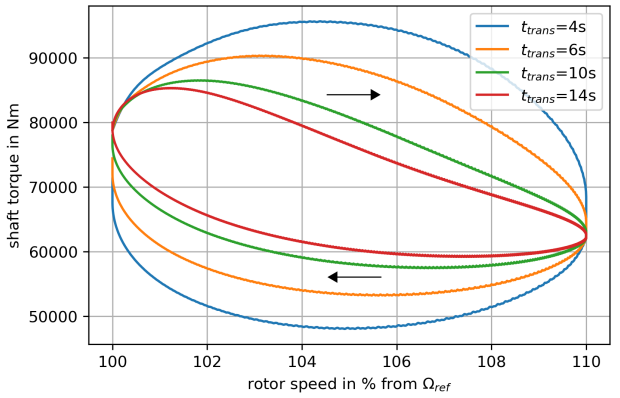


FIG 9. shaft torque during rotor speed variation for high blade loading condition, $C_T/\sigma = 0.125$ and $\mu = 0.2$

illustrates the progression of shaft torque during transition to the optimum rotor speed. Since the decrease in torque surpasses the increase in rotor speed, a reduction in power consumption of $\Delta P_{shaft} = 15.89\,\%$ is achieved. For the acceleration of the rotor with a transition time of $t_{trans} = 2\,\mathrm{s}$, the shaft torque reaches a maximum value of $96\,000\,\mathrm{N\,m}$. In this case the increased load on the shaft may exceed the limit of the structural design. This issue can be resolved by directing the controller design to prescribe longer transition times, which should not pose an issue since no resonance crossing was observed for rotor speeds above reference speed (cf. fig. 5).

## 4. COMPOUND SPLIT MODULE

The proposed gear design requires active control in order to be able to fully utilize all advantages (Ref. [14]). Furthermore, a method for active damping of the drive train for the entire speed range should be designed. Active damping of a drive train is illustrated in Ref. [15], where a simple dynamic rotor model is also considered. The schematic of the compound split (CS) is shown in fig. 10. The CS consists of the serially connected planetary gears and the two electric motors. The kinematics of the system are reduced to the control relevant states $\omega_s$ and $\omega_{C2}$ and shown in eq. 5.

$$(5)\qquad \begin{bmatrix} \omega_s \\ \omega_{EM} \\ \omega_{p1} \\ \mathrm{v}_{p1} \\ \omega_{EG} \\ \omega_{C2} \\ \mathrm{v}_{p2} \\ \omega_{p2} \end{bmatrix} = \begin{bmatrix} 1 & 0 \\ -\frac{r_{s1}r_{R2}+2r_{C1}r_{s2}}{r_{R1}r_{R2}i_{EM}} & \frac{4r_{C1}r_{C2}}{r_{R1}r_{R2}} \\ -\frac{r_{s1}r_{R2}+r_{C1}r_{s2}}{r_{p1}r_{R2}} & \frac{2r_{C1}r_{C2}}{r_{R2}r_{p1}} \\ -\frac{r_{s2}r_{C1}}{r_{R2}} & \frac{2r_{C2}r_{C1}}{r_{R2}} \\ -\frac{r_{s2}}{r_{R2}i_{EG}} & \frac{2r_{C2}}{r_{R2}i_{EG}} \\ 0 & 1 \\ 0 & r_{C2} \\ -\frac{r_{s2}}{r_{p2}} & \frac{r_{C2}}{r_{p2}} \end{bmatrix} \begin{bmatrix} \omega_s \\ \omega_{C2} \end{bmatrix}$$

To get the differential functions for this model the Lagrange method is applied. For this reason, the kinetic and potential energy is needed

$$(6)\qquad \mathrm{T} = \sum_i M_{red\,i} \cdot q_i$$

$M_{red\,i}$ are the reduced masses for the degree of freedom of $q_i$.
The total kinetic energy $T_{kin}$ of the system is

$$(7)\qquad \begin{aligned} \mathrm{T} = \frac{1}{2}[&J_{eng}\omega_{eng}^2 + J_{G11}w_d^2 + (J_{G12} + J_{s1} + J_{s2})\omega_s^2 \\ &+ J_{C1}w_{C1}^2 + J_{p1}w_{p1}^2 + m_{p1}\mathrm{v}_{p1}^2 + J_{R1}w_{R1}^2 \\ &+ J_{EM}w_{EM}^2 + (J_{C2} + J_{G22})\omega_{C2}^2 + J_{p2}w_{p2}^2 + m_{p2}\mathrm{v}_{p2}^2 \\ &+ J_{R2}w_{R2}^2 + J_{EG}w_{EG}^2 + J_{G21}w_M^2 + J_R\omega_R^2] \end{aligned}$$

The potential energy of the torsion springs with stiffness $k_i$ is given by

$$(8)\qquad \mathrm{V} = \frac{1}{2}(k_{s1}\Delta\varphi_{ed}^2 + k_{s2}\Delta\varphi_{MR}^2)$$

The generalized forces $Q_i$ are obtained by the virtual work through virtual displacements along the generalized coordinates:

$$(9)\qquad \delta\mathrm{A} = \sum_i Q_i \cdot \delta q_i$$

Therefore the virtual work in the system is determined to

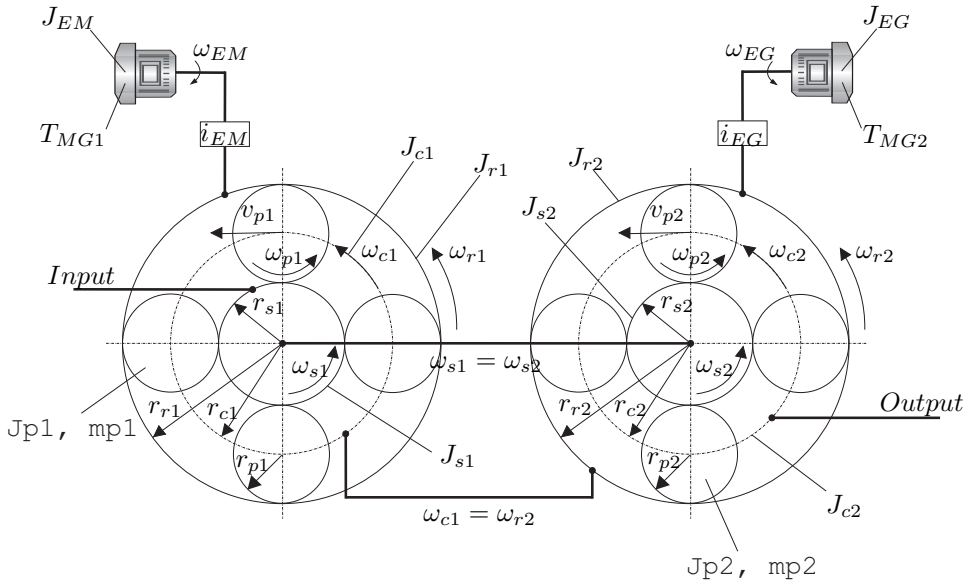


FIG 10. Schematic of the compound split module and the power drive units

$$
\begin{aligned}
\delta \mathrm{A} = {} & \delta\varphi_{eng}\,(T_{eng} - d_{s1}\Delta\dot{\varphi}_{ed} - d_{s4}\dot{\varphi}_{eng}) \\
& + \delta\varphi_s\,(-\frac{T_{MG1}(r_{s1}r_{R2} + 2r_{C1}r_{s2})}{i_{EM}r_{R1}r_{R2}} \\
& + \frac{d_{s1}\Delta\dot{\varphi}_{ed}}{i_{G1}} - \frac{d_{s2}\Delta\dot{\varphi}_{MR}}{i_{G2}} - \frac{T_{MG2}r_{s2}}{r_{R2}i_{EG}}) \\
& + \delta\varphi_{C2}\,(\frac{4T_{MG1}r_{C1}r_{C2}}{r_{R1}r_{R2}i_{EM}} + \frac{2T_{MG2}r_{C2}}{r_{R2}i_{EG}}) \\
& + \delta\varphi_R\,(T_{load} + d_{s2}\Delta\dot{\varphi}_{MR})
\end{aligned} \tag{10}
$$

In order to describe the behavior of the system, the Lagrangian equations with the generalized coordinates are introduced:

$$
\frac{d}{dt}(\frac{\partial T}{\partial \dot{q}_i}) - \frac{\partial T}{\partial q_i} + \frac{\partial V}{\partial q_i} = Q_i \tag{11}
$$

By inserting the derivations of the equations for kinetic energy and potential energy into the Lagrangian equations, the resulting differential equations describe the motion of the respective system:

$$
M(q)\ddot{q} + C(q)\dot{q} + Kq = 0 \tag{12}
$$

Considering $(\varphi_{ed} - \varphi_{eng}) = \Delta\varphi_1 = x_1$ and $(\varphi_M - \varphi_R) = \Delta\varphi_2 = x_2$ the chosen state-, input- and disturbance-vector yields to

$$
\begin{aligned}
x &= [\Delta\varphi_1\ \Delta\varphi_2\ \omega_{eng}\ \omega_s\ \omega_{C2}\ \omega_R]^T, \\
u &= [T_{eng}\ T_{MG1}\ T_{MG2}]^T, \\
z &= [T_{load}]^T,
\end{aligned} \tag{13}
$$

After applying the kinematic bounds in the Lagrangian equations and deriving the functions, the succeeding system description is determined. The system can be expressed in state space description as follows:

$$
\begin{aligned}
\dot{x} &= \boldsymbol{Ax} + \boldsymbol{Bu} + \boldsymbol{ez} \\
y &= \boldsymbol{Cx}
\end{aligned} \tag{14}
$$

## 5. OVERVIEW OF CONTROL ARCHITECTURE

The Compound split gear is controlled by a LQR control design using the modal weighting method. The oscillating modes are the ones that will be damped with the control design.
The input weighting matrix $R$ is defined in a manner that the torque inputs will be equal for both electric motors.
The control law in the steady state is defined as follows:

$$
u_\infty = -Kx_\infty + K_w w_\infty + K_z z_\infty \tag{15}
$$

For steady state of the system ($\dot{x} = 0$), the system description from eq. 14 is rearranged and the result for the state vector is $x_\infty$, eq. 16 and for the controlled variable is $y_\infty$ , eq. 17.

$$
x_\infty = -(A - BK)^{-1}[BK_w w + (BK_z + e)z_\infty] \tag{16}
$$

$$
y_\infty = Cx_\infty = -C(A-BK)^{-1}[BK_w w + (BK_z + e)z_\infty] \tag{17}
$$

For the disturbance response $w_\infty = 0$ is set to zero

$$
-C(A - BK)^{-1}(BK_z + e) = 0 \tag{18}
$$

and the control gain $K_z$ is formulated as

$$
K_z = C(A - BK)^{-1}e[-C(A - BK)^{-1}B]^{-1} \tag{19}
$$

, determining the matrix $K_w$. To obtain the pre-gain, eq. 16 is inserted into eq. 15:

$$u_\infty = \underbrace{[-K(BK - A)^{-1}B + I]}_{\psi_u} K_w w_\infty \tag{20}$$

, obtaining together with eq. 15 the new control description:

$$u_\infty = \psi_u K_w w_\infty + \psi_z z_\infty \tag{21}$$

For the reference response, $z_\infty = 0$ is applied:

$$y_\infty := w_\infty \tag{22}$$

Finally $K_w$ is determined as

$$Iw_\infty = \underbrace{C(BK - A)^{-1}B}_{\psi_y} K_w w_\infty \tag{23}$$

$$I = \psi_y K_w \tag{24}$$

Eq. 24 is only valid for a single steady state point, therefore the control law has to be updated at every time step.

$$K_w = \underbrace{\psi_y^+}_{\text{pseudo Inverse}} \tag{25}$$

To optimize the control response, the control law could be extended with a feed-forward control.

## 6. COUPLED ROTOR-CS SIMULATION

The co-simulation environment of Simulink with embedded Dymore is used to apply the control solution to the high-fidelity helicopter rotor system. Simulink handles control algorithms and simulation of the compound split module, while Dymore handles the detailed rotor dynamics, including blade flexibility and aerodynamics. This combined approach enables efficient analysis and optimization of the entire drive train system performance. Fig. 13 shows the co-simulation of the control system where one block describes the analytical model of the compound split gear, one block includes the high-fidelity helicopter rotor and one block contains the different control solutions, here the LQR solution outlined in the previous section.
As also seen in the lower left part of fig. 13, the offline calculated optimal reference speed is selected based on the current flight state within the flight envelope.
The time-stepping scheme of the simulation framework is set to a fixed time step of $\Delta t = 0.001\,\text{sec}$. It is inherited by the Dymore rotor model block. This approach ensures consistent coupling between the compound split gear and the rotor at every time step. The coupling between these two models is done by prescribing the output shaft speed of the compound split to the rotor shaft of the Dymore block. The shaft torque of the rotor is subsequently fed back to the compound split model, expressed as the disturbance $z$ in the state-space system in eq. (13).
As a first step, a simulation of the isolated rotor block without coupling to the compound split is carried out within the Simulink framework. The rotor shaft torque spectrum is analyzed and compared with the fan plot in fig. 5. Since the fan plot was generated by a modal analysis of the rotor model neglecting any aerodynamic effects, the aerodynamic model is also turned off in the Dymore block for this simulation. In both cases, the blade lag damper is also neglected. To analyze the torque spectrum, the rotor is excited by a collective pulse for $\Delta t = 0.001\,\text{s}$. The Fast Fourier Transform (FFT) of the shaft torque signal with a frequency resolution of $\Delta f = 0.22\,\text{Hz}$ is shown in fig. 11.
The peaks of the FFT are compared to the eigenfrequencies of the blade modes at $\Omega_{ref} = 4.3\,\text{Hz}$ in the fan plot [fig. 5]. For better readability, the eigenfre-

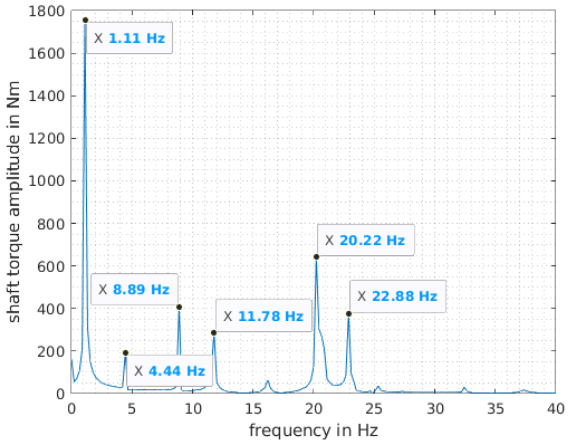


FIG 11. FFT of rotor shaft torque excited by collective pulse neglecting aerodynamics and lag damper

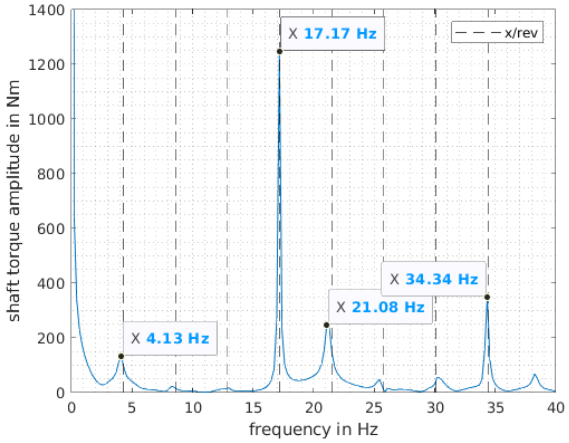


FIG 12. FFT of rotor shaft torque during forward flight in coupled simulation

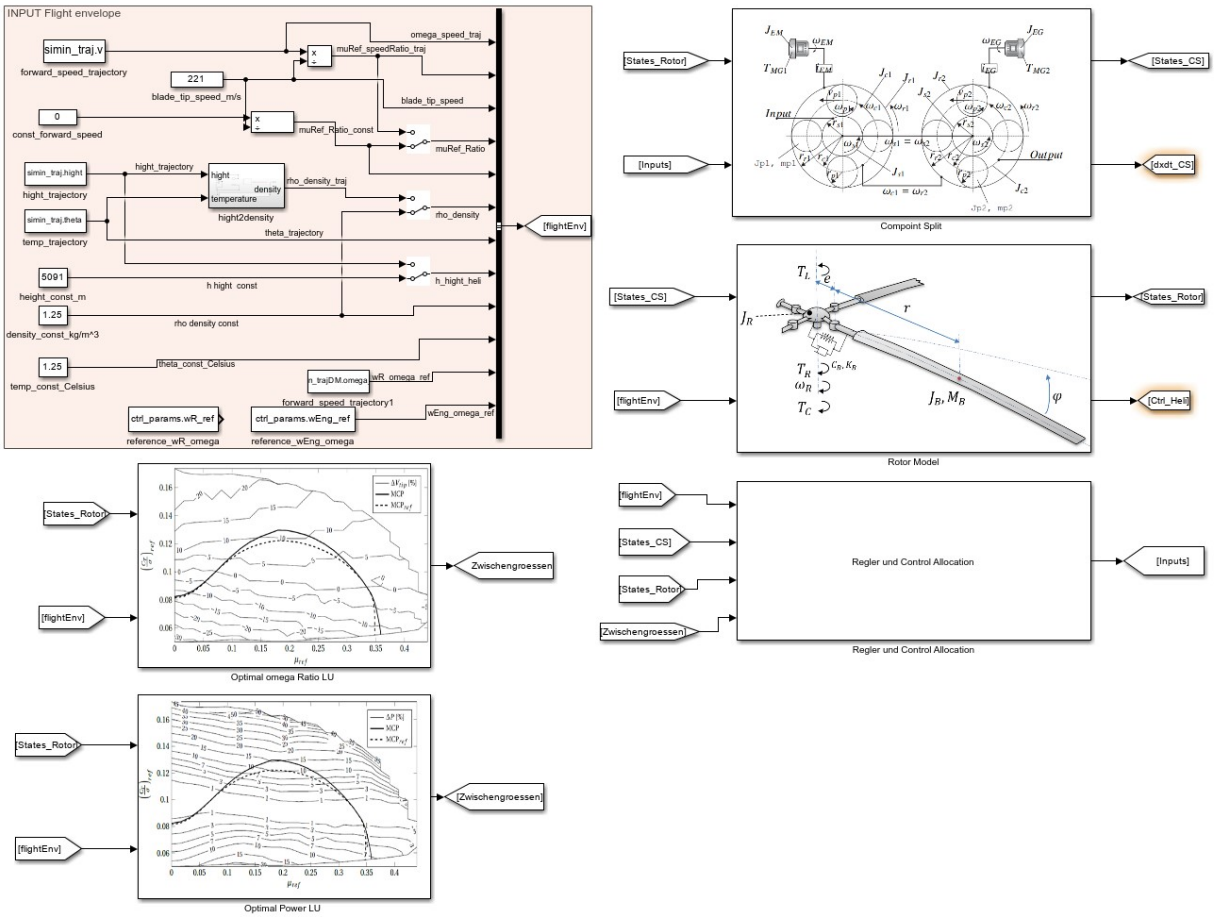


FIG 13. Co-simulation of Dymore rotor model, compound split and control model

quencies in the fan plot are normalized to the reference rotor speed, $\nu_{blade} = f_{blade}/\Omega_{ref}$. It can be seen that all the fundamental blade modes, i.e. lead-lag (1.14 Hz, 20.19 Hz), flap (4.44 Hz, 12.22 Hz) and torsion modes (22.88 Hz) have an impact on the shaft torque and correspond to the peaks of the FFT. The peak at 8.89 Hz is probably a multiple of the first flap mode.

In the second step, the Dymore rotor block is coupled with the compound split model within the Simulink framework. For this simulation, a horizontal forward flight condition with advance ratio of $\mu = 0.149$, corresponding to the flight counter c8513 of the UH-60A airloads catalog [16], is selected. The blade lag dampers and Peter's aerodynamics (cf. sec. 3) are considered. The rotor is trimmed to a blade loading of $C_T/\sigma = 0.079$ according to the c8513 flight condition. Similar to the previous simulation, the rotor is excited by a collective step input in the trimmed state. The FFT response of the shaft torque is shown in fig. 12. Multiples of the rotor speed are represented by a dashed line. Compared to the simulation excluding aerodynamic effects, the predominant peaks in the shaft torque are now attributed to aerodynamic excitation rather than blade modes. Since the UH60-A is a four-bladed rotor, the principal excitation frequency is $f = 4 \cdot \Omega_{ref} = 17.2$ Hz. This frequency aligns with the prominent peak observed in fig. 12. The peak at $f = 21.08$ Hz does not perfectly correspond to the 5/rev frequency, suggesting a potential interference with the collective lag mode at $f = 20.19$ Hz.

The FFT analysis of the shaft torque in forward flight condition indicates that active damping measures should be implemented to mitigate the x/rev oscillations and their interference with the collective lag mode.

## 7. CONCLUSION

Research conducted on variable speed rotors indicates that significant power savings of up to 20 % can be achieved by dynamically adjusting the main rotor speed according to the current flight state. By adjusting the rotor speed, an optimum mean angle of attack of the blades can be attained, resulting in reduced drag. The transition time between different rotor speed levels must be carefully managed to be fast enough to prevent resonance, but slow enough to avoid exceeding the structural shaft torque limit.

The continuous variable transmission is realized by a compound split gear design that integrates two electrical variators. Utilizing these highly dynamic electric machines enables the feasibility of actively damping rotor shaft oscillations.

By setting up a multi-domain simulation framework, the whole drive train dynamics of the coupled compound split gear and the rotor is investigated. The

examination of the rotor shaft torque within the frequency spectrum reveals that the primary peaks originate from multiples of the rotor speed frequency, coupled with its interaction with the collective rotor blade lag modes.
In order to fully utilize the capabilities of the electric variators for active damping, integrating a battery storage unit as an auxiliary buffer could be beneficial. This setup would enable the excess electrical energy produced by the generator to be utilized by the engine for vibration damping purposes.
Subsequently, integration of the rotor pitch control into the rotor speed variation control could be considered. Given the prior understanding that blade pitch adjustment is required to maintain a trimmed flight state with changes in rotor speed, integrating the rotor collective into the control loop using a feedforward control algorithm is a plausible approach.
In a next step, the developed compound split gear model and its active control design will be integrated into the rotorcraft simulator ROSIE at the Institute of Helicopter Technology. A pilot test campaign will be conducted to assess various concepts of variable rotor speed actuation, with a specific emphasis on evaluating handling qualities.

## ACKNOWLEDGMENT

This work is supported by the German Federal Ministry for Economic Affairs and Climate Action through the German Aviation Research Program LuFo VI-1 and the Austrian Research Promotion Agency through the Austrian Research Program TAKE OFF. The paper is a result of the transnational project "Varispeed II".


Contact address:

j.koch@tum.de

## References

[1] Garre, Amri, Pflumm, Paschinger, Mileti, Hajek, and Weigand. Helicopter Configurations and Drive Train Concepts for Optimal Variabel Rotor-Speed Utilization. In DLRK, 2016.

[2] W Garre, T Pflumm, and M Hajek. Enhanced Efficiency and Flight Envelope by Variable Main Rotor Speed for Different Helicopter Configurations. In Proceedings of the 42st European Rotorcraft Forum, 2016.

[3] Scheu, Thomas, Poks, Agnes, Donner, Florian, and Weigand, Michael. Dynamic Simulation of a Rotorcraft Main Transmission with Continuous Variable Ratio. 2023.

[4] A. Hopkins and Gene Ruzicka. Analytical Investigations of Coupled Rotorcraft Drive Train Dynamics. 1995.

[5] Stacy Sidle, Ananth Sridharan, and Inderjit Chopra. Coupled Vibration Prediction of Rotor-Airframe-Drivetrain-Engine Dynamics. 2018.

[6] Felix Weiss and Christoph Kessler. Drivetrain influence on the lead–lag modes of hingeless helicopter rotors. 2020.

[7] Felix Armin Weiß. Einfluss des Triebstrangs auf die Schwenkbewegung von Hubschrauberrotoren. 2022.

[8] Bischläger, Mario, Gross, Christopher, Koch, Jonas, Poks, Agnes, and Weigand, Michael. Dynamic Simulation of a rotor system with Variable speed. 2022.

[9] O. A. Bauchau. Flexible Multibody Dynamics. Solid Mechanics and Its Applications. Springer Netherlands, 2011.

[10] Peters and He. Finite State Induced Flow Models Part II - Three-Dimensional Rotor Disk. 1995.

[11] William G. Bousman. Aerodynamic Characteristics of SC1095 and SC1094 R8 Airfoils:. Technical report, Defense Technical Information Center, 2003.

[12] D. Peters. A state-space airloads theory for flexible airfoils. 2007.

[13] Ruthvik Chandrasekaran and Dewey H. Hodges. Performance Advantages and Resonance Analysis of a Variable Speed Rotor Using Geometrically Exact Beam Formulations. Journal of the American Helicopter Society, 2021.

[14] Willem Rex, Tobias Pflumm, and Manfred Hajek. Uh-60a rotor and coupled rotor-fuselage simulation framework validation and analysis.

[15] Yong Wang, Qiangang Zheng, Haibo Zhang, and Haoying Chen. Research on predictive control of helicopter/engine based on lms adaptive torsional vibration suppression. Journal of Low Frequency Noise, Vibration and Active Control, 37(4):1151–1163, 2018.

[16] William G. Bousman and Robert M. Kufeld. UH-60A Airloads Catalog. NASA/TM-2005-212827, 2005.